

Tunnel-Type $\text{Na}_2\text{Ti}_6\text{O}_{13}$ @Carbon Nanowires as Anode Materials for Low-Temperature Sodium-Ion Batteries

Qing-Song Lai⁺^[a], Jian-Jia Mu⁺^[a], Zhao-Meng Liu,^[a] Lu-Kang Zhao,^[a] Xuan-Wen Gao,^{*[a]}, Dong-Run Yang,^[a] Hong Chen,^[a] and Wen-Bin Luo^{*[a]}

Economical efficient anode materials play an important role in low-temperature sodium-ion batteries (SIBs). Tunnel-type structured $\text{Na}_2\text{Ti}_6\text{O}_{13}$ @C nanowires were synthesized and utilized as anode material for low-temperature SIBs. The appropriate interlayer spacing for sodium ion insertion and short diffusion pathway can accelerate the sodium ion kinetics and decrease the apparent activation energy at low temperature. The diffusion apparent activation energy and activation energy for $\text{Na}_2\text{Ti}_6\text{O}_{13}$ @C were calculated to be 42.0 kJ mol^{-1} and

15.3 kJ mol^{-1} with the sodium ion diffusion coefficients about $10^{-12} \text{ cm}^2 \text{s}^{-1}$. The $\text{Na}_2\text{Ti}_6\text{O}_{13}$ @C nanowires exhibit a high reversible capacity of 100 mAh g^{-1} at 0°C with 99.6% retention after 200 cycles at 0.5 C . Coupling with the sodium vanadium phosphate as cathode, the assembled $\text{Na}_2\text{Ti}_6\text{O}_{13}$ @C || NVP full-cell can keep a 65% capacity retention after 175 cycles at 0°C . This work presents that $\text{Na}_2\text{Ti}_6\text{O}_{13}$ @C nanowires can be an ideal type of anode active materials for low-temperature SIBs.

Introduction

Sodium-ion batteries (SIBs) have been gradually considered as one of the most prominent candidates for large-scale energy storage systems due to the abundant sodium resources, high economic utility and environmental friendliness.^[1–5] Although possessing a satisfactory reversible capacity and excellent cycle stability at room working temperature during long-term global research, the electrochemical performance will be dramatically decreased once the ambient temperature falling to below 0°C . Multitudinous research investigations were conducted to enhance the low-temperature electrochemical performance by the electrolyte modification strategy, such as adding additives to reduce the freezing point of the electrolyte^[6,7] and replacing solute salts to increase ionic conductivity.^[8] However, these design principles cannot absolutely satisfy the requirements of most cases at low working temperature. In fact, the anode material option and optimization play an important role in determining the low-temperature electrochemical performance. It is well-known that the widely employed hard carbon anode is not suitable for the low working temperature owing to the sluggish reaction kinetics of ions diffusion.^[2,3,9,10] Therefore, exploring alternative anode materials for large-scale energy storage with wide working temperature is urgent to overcome

current existing challenges for the practical application field, particularly at low working temperature.^[11–16]

Inspired by lithium-ion batteries, titanium oxide-based anode materials, such as $\text{Na}_2\text{Ti}_n\text{O}_{2n+1}$ ($2 \leq n \leq 9$), exhibit an infusive theoretical specific capacity and a stable cycle performance in a wide-range working temperature.^[17–26] Among these sodium titanite oxides, the tunnel-type structured $\text{Na}_2\text{Ti}_6\text{O}_{13}$, a three-dimensional chain-arrangement of $[\text{TiO}_6]$ octahedrons in a relative larger layered structure, attracted a focused attention owing to the inherent advantages of the high ionic mobility and the low ion migration impedance. In order to optimize the ion diffusion behavior, herein, one-dimensional $\text{Na}_2\text{Ti}_6\text{O}_{13}$ @C nanowires were designed and synthesized for the low-temperature SIB. The $\text{Na}_2\text{Ti}_6\text{O}_{13}$ @C nanowires can not only effectively accelerate the ion diffusion dynamics, but also decrease the sodium ion transport activation energy at low working temperature. The corresponding diffusion apparent activation energy and the activation energy were gained for 42.0 kJ mol^{-1} and 15.3 kJ mol^{-1} . The Na^+ diffusion coefficients keep a similar trend in the range of between 20°C and 0°C . The $\text{Na}_2\text{Ti}_6\text{O}_{13}$ @C displays a pleasant specific capacity and a favorable long-term behavior in the working temperature range from 25°C to -20°C . Coupling with sodium vanadium phosphate $[\text{Na}_3\text{V}_2(\text{PO}_4)_3]$ as cathode, the sodium-ion full cell ($\text{Na}_2\text{Ti}_6\text{O}_{13}$ @C || $\text{Na}_3\text{V}_2(\text{PO}_4)_3$) exhibits a conspicuous 65% capacity retention after 175 cycles at 0°C . It is hoped that the proposed tunnel-type $\text{Na}_2\text{Ti}_6\text{O}_{13}$ @C nanowire for SIBs can be promising active materials for the low-temperature energy storage system.

Results and Discussion

The detailed experimental information can be seen in the Support Information. As shown in Figures 1 and S1, the field emission scanning electron microscope (FESEM) patterns of

[a] Q.-S. Lai,⁺ J.-J. Mu,⁺ A/Prof. Z.-M. Liu, L.-K. Zhao, A/Prof. X.-W. Gao, D.-R. Yang, H. Chen, Prof. W.-B. Luo
Institute for Energy Electrochemistry and Urban Mines Metallurgy
School of Metallurgy
Northeastern University
Shenyang, Liaoning 110819 (China)
E-mail: gaoxuanwen@mail.neu.edu.cn
luowenbin@smm.neu.edu.cn

[+] These authors contributed equally to this work.

Supporting information for this article is available on the WWW under
<https://doi.org/10.1002/batt.202200549>

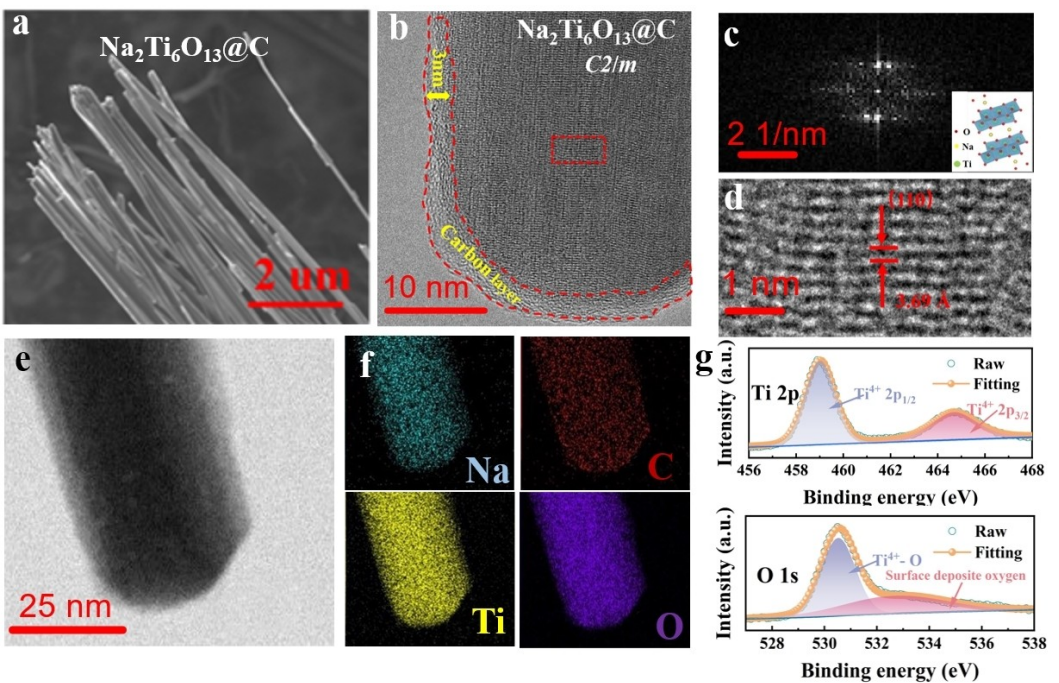


Figure 1. a) The SEM pattern of $\text{Na}_2\text{Ti}_6\text{O}_{13}@\text{C}$ composite; b) HR-TEM images of $\text{Na}_2\text{Ti}_6\text{O}_{13}@\text{C}$ nanowires; c) the corresponding fast Fourier transform (FFT) pattern; d) the corresponding inverse Fourier transform (IFFT) pattern. e and f) Elemental mapping of a single $\text{Na}_2\text{Ti}_6\text{O}_{13}@\text{C}$ nanorod. g) The XPS spectra of Ti 2p and O 1s of $\text{Na}_2\text{Ti}_6\text{O}_{13}@\text{C}$.

TiO_2 , Pre- $\text{Na}_2\text{Ti}_6\text{O}_{13}$, bare $\text{Na}_2\text{Ti}_6\text{O}_{13}$ and $\text{Na}_2\text{Ti}_6\text{O}_{13}@\text{C}$ composite are illustrated. The obtained $\text{Na}_2\text{Ti}_6\text{O}_{13}@\text{C}$ nanowires keep a uniform one-dimensional structure with a length of about 6 μm and a diameter of 20 nm. Figure S2 displays the XRD patterns of the $\text{Na}_2\text{Ti}_6\text{O}_{13}$, which is indexed to the space group C2/m. As shown in Figure 1(b), the even carbon layer with thickness of 3 nm was successfully coated on $\text{Na}_2\text{Ti}_6\text{O}_{13}$ surface, which can guarantee the electronic conductivity and structure stability. Figure 1(c and d) demonstrates the corresponding fast Fourier transform (FFT) pattern, which supplied legible (110) $\text{Na}_2\text{Ti}_6\text{O}_{13}@\text{C}$ lattice fringes with the interplanar spacing of 3.69 \AA . This interplanar spacing is three times than that of the ionic radius of Na^+ (0.102 nm), which can efficiently facilitate sodium ions diffusion and insertion/extraction.^[27–29] The Na, Ti, O and C elements distribution (Figure 1f) shows a well-proportioned distribution over the whole individual nanowire area. The X-ray Photoelectron Spectroscopy (XPS) is further used to explore chemical bonding and valence states of different elements in the $\text{Na}_2\text{Ti}_6\text{O}_{13}@\text{C}$ nanowires (Figure 1g). The Ti 2p peaks were deconvoluted into peaks located at 459.0 eV and 464.7 eV, which has a valence state (Ti^{4+}) in $\text{Na}_2\text{Ti}_6\text{O}_{13}@\text{C}$ nanowires. The O 1s is consisted of 530.52 eV and 532.73 eV on behalf of $\text{Ti}^{4+}-\text{O}$ bond. It is concluded that the tunnel-type structured $\text{Na}_2\text{Ti}_6\text{O}_{13}@\text{C}$ nanowires can be obtained with a one-dimensional high crystal orientation.

The electrochemical properties of $\text{Na}_2\text{Ti}_6\text{O}_{13}@\text{C}$ and $\text{Na}_2\text{Ti}_6\text{O}_{13}$ were tested as shown in Figure 2. The $\text{Na}_2\text{Ti}_6\text{O}_{13}@\text{C}$ displays a superior rate capability of 146.2 mAh g^{-1} , 137.2 mAh g^{-1} , 125.3 mAh g^{-1} , 114.6 mAh g^{-1} at various rates of 0.1 C, 0.2 C, 0.5 C and 1 C, respectively (Figure 2a). Rate

capability of $\text{Na}_2\text{Ti}_6\text{O}_{13}@\text{C}$ at 0 °C was analyzed as well (Figure 2b). It reveals 120 mAh g^{-1} , 92 mAh g^{-1} , 65 mAh g^{-1} , and 50 mAh g^{-1} at 0.1, 0.2, 0.5 and 1 C, respectively. The ability of tolerance sudden change temperature is important for practical application at the wide working temperature. The charge/discharge curves at 0.1 C of $\text{Na}_2\text{Ti}_6\text{O}_{13}@\text{C}$ from 0 °C to -40 °C were demonstrated in Figure S3. In a low-temperature series testing, the $\text{Na}_2\text{Ti}_6\text{O}_{13}@\text{C}$ anode delivered a specific capacity of 40.2 mAh g^{-1} when the ambient temperature was suddenly decreased to -40 °C (Figure S3), and was restored to 150.5 mAh g^{-1} at 0 °C. It proves that the $\text{Na}_2\text{Ti}_6\text{O}_{13}@\text{C}$ nanowires have the adaptability for rapid temperature change. Lifespan for batteries in daily life is important, especially in extreme conditions. As shown in Figure 2(c), the $\text{Na}_2\text{Ti}_6\text{O}_{13}@\text{C}$ nanowires maintain an exceptional steady long-term cycle, providing an excellent specific capacity of 97.2 mAh g^{-1} at 0.2 C after 200 cycles. To further understand and analyze the mechanism for the excellent stability of $\text{Na}_2\text{Ti}_6\text{O}_{13}@\text{C}$ nanowires, the XRD, SEM and TEM images after a long cycling test were studied. In Figure S4, the XRD detection shows that the peak positions before and after 200 cycles have no obvious deviation and disappearance. In Figure S5, the SEM images before and after 200 cycles showed that the morphology of $\text{Na}_2\text{Ti}_6\text{O}_{13}@\text{C}$ materials do not change and the nanowires do not have obvious fragmentation phenomenon. In Figure S6, the HR-TEM of $\text{Na}_2\text{Ti}_6\text{O}_{13}@\text{C}$ after 200 cycles shows that the carbon layer remains intact after cycling. In summary, the structure and morphology of $\text{Na}_2\text{Ti}_6\text{O}_{13}@\text{C}$ keep stable before and after cycles, which explains that $\text{Na}_2\text{Ti}_6\text{O}_{13}@\text{C}$ have better cycling performance. Figure 2(d) reveals that the $\text{Na}_2\text{Ti}_6\text{O}_{13}@\text{C}$ nanowires

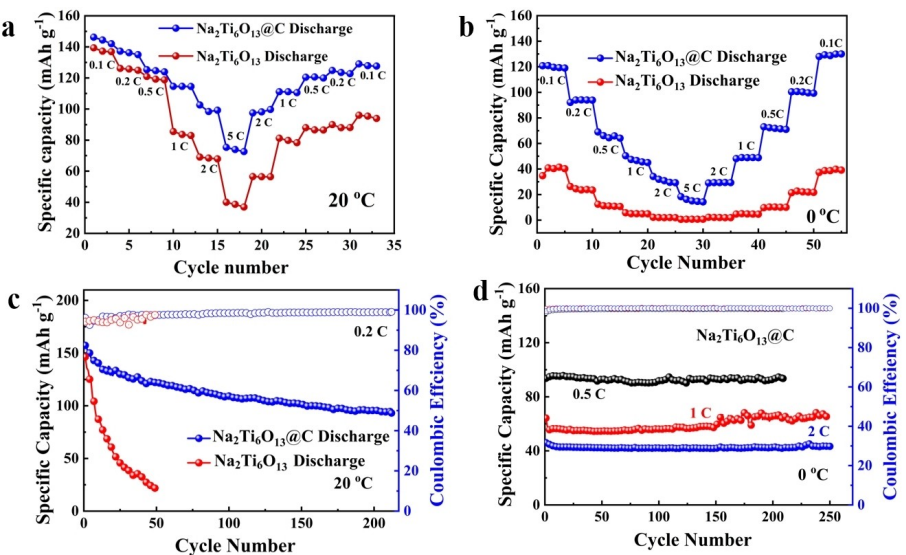


Figure 2. a) Rate performance of the $\text{Na}_2\text{Ti}_6\text{O}_{13}$ and $\text{Na}_2\text{Ti}_6\text{O}_{13}@\text{C}$ from 0.1 C to 5 C at 20 °C; b) Rate performance of $\text{Na}_2\text{Ti}_6\text{O}_{13}$ and $\text{Na}_2\text{Ti}_6\text{O}_{13}@\text{C}$ from 0.1 C to 5 C at 0 °C. c) Cycling performance of the $\text{Na}_2\text{Ti}_6\text{O}_{13}$ and $\text{Na}_2\text{Ti}_6\text{O}_{13}@\text{C}$ at 0.2 C. d) Cycle performance of $\text{Na}_2\text{Ti}_6\text{O}_{13}@\text{C}$ from 0.5 C, 1 C and 2 C at 0 °C.

maintained an excellent capacity retention of 99.9% after 200 cycles at 0.5 C and 93.4% after 250 cycles at 2 C under 0 °C. Combining the above results, it demonstrates that the obtained $\text{Na}_2\text{Ti}_6\text{O}_{13}@\text{C}$ nanowires can provide an acceptable low temperature electrochemical performance including rate capability and cycling lifespan compared to other previously reported low temperature anodes (Table S1).

The ion diffusion behaviors of $\text{Na}_2\text{Ti}_6\text{O}_{13}@\text{C}$ and $\text{Na}_2\text{Ti}_6\text{O}_{13}$ were evaluated by a variety of electrochemical tests as shown in Figure 3. The cyclic voltammograms (CV) curves of $\text{Na}_2\text{Ti}_6\text{O}_{13}$ and $\text{Na}_2\text{Ti}_6\text{O}_{13}@\text{C}$ at different scanning rates at 20 °C are shown in Figure 3(a). An anodic peak located at 0.15 V of $\text{Na}_2\text{Ti}_6\text{O}_{13}$ was distinctly observed at first discharge process and faded in the following cycles, corresponding to the solid electrolyte layer (SEI) formation.^[30] Moreover, the cathodic peak situated at 0.57 V indicates the rapid extraction process of Na^+ . The cathodic peak shifts to 0.74 V with the current density increasing, manifesting the emergence of serious polarization phenomenon from the structural deformation of $\text{Na}_2\text{Ti}_6\text{O}_{13}$. By contrast, the cathodic peak of $\text{Na}_2\text{Ti}_6\text{O}_{13}@\text{C}$ in Figure 3(b) situated at 0.68 V has a negligible skewing with current densities increasing, certifying that the thin carbon layer coating can effectively accelerate the ion kinetics rate and alleviate the structural damage. The redox peaks located at 0.8/1.1 V are related with the characteristic redox pairs of tunnels $\text{Na}_2\text{Ti}_6\text{O}_{13}$ and the redox peaks located at 1.2/1.3 V are consistent with $\text{Ti}^{4+}/\text{Ti}^{3+}$ redox reaction. The electrochemical impedance spectroscopy (EIS) in Figure 3(c, d) at different temperatures (20 °C, 30 °C, 40 °C, 50 °C, 60 °C) were conducted to calculate the diffusion coefficient and apparent activation energies.^[31–33] As shown in Figure 3(e) the diagram of $\log D$ as a function of T^{-1} , according to Z_{re} versus $\omega^{1/2}$ at different temperatures (Figure S7), the diffusion apparent activation energy (E_{ad}) can be gained for 42.0 and 61.6 kJ mol⁻¹ of the $\text{Na}_2\text{Ti}_6\text{O}_{13}@\text{C}$ and $\text{Na}_2\text{Ti}_6\text{O}_{13}$. The E_{ad} of $\text{Na}_2\text{Ti}_6\text{O}_{13}@\text{C}$ and $\text{Na}_2\text{Ti}_6\text{O}_{13}$

were gained as well for 15.3 and 46.6 kJ mol⁻¹ (Figure 3f). $\text{Na}_2\text{Ti}_6\text{O}_{13}@\text{C}$ has a lower apparent activation energy compared with the $\text{Na}_2\text{Ti}_6\text{O}_{13}$, which is ascribed to the one-dimensional structure and homogeneous thin carbon layer coating.^[34] It has been proved that the decreased Na^+ diffusion barrier and low activation energy can make a significant promotion to the performance.^[35]

To further reveal the Na^+ dynamics at the low working temperature, the galvanostatic intermittent titration technique (GITT) (Figure 4a–d) was employed to further analyze sodium ion kinetic behavior.^[36,37] According to Fick's second law, the diffusion process of Na^+ is an unsteady diffusion.^[38,39] The graph of voltage as a function of specific capacity of $\text{Na}_2\text{Ti}_6\text{O}_{13}$ and $\text{Na}_2\text{Ti}_6\text{O}_{13}@\text{C}$ at 0 °C and 20 °C were obtained from the GITT test (Figure S8). The diffusion coefficients as a function of time were plotted in Figure 4(a, b, e, f). The charging diffusion coefficients (D_{Na^+}) for $\text{Na}_2\text{Ti}_6\text{O}_{13}@\text{C}$ is about $10^{-12} \text{ cm}^2 \text{s}^{-1}$ at 20 °C and maintained at 0 °C, much higher than those of $\text{Na}_2\text{Ti}_6\text{O}_{13}$. Combining the above results, the surface carbon has a positive effect to electrochemical behavior of $\text{Na}_2\text{Ti}_6\text{O}_{13}$ electrode by improving the sodium ions diffusion coefficient at low working temperature. The ion transport in the anode-electrolyte interface plays a critical role in the low working temperature and monitored by in-situ electrochemical EIS. The $\text{Na}_2\text{Ti}_6\text{O}_{13}$ and $\text{Na}_2\text{Ti}_6\text{O}_{13}@\text{C}$ in Figure 3(c, d, e, h) at 20 °C and 0 °C were employed to elucidate the interphase on transport kinetics. The experimental data were collected by the equivalent circuits. Specific fitting parameters are obtained and listed in Tables S2 and S3. The high charge-transfer resistance (R_{ct}) of $\text{Na}_2\text{Ti}_6\text{O}_{13}$ was acquired by calculation between 184.7 Ω and 782.8 Ω at 20 °C, which was originated from the slower ion transport. Comparing with $\text{Na}_2\text{Ti}_6\text{O}_{13}$, the charge-transfer resistance of $\text{Na}_2\text{Ti}_6\text{O}_{13}@\text{C}$ was directly reduced to between 66.36 Ω and 568.9 Ω. The maximum R_{ct} of $\text{Na}_2\text{Ti}_6\text{O}_{13}$ (6.6 kΩ) measured at 0 °C is two times higher than that of $\text{Na}_2\text{Ti}_6\text{O}_{13}@\text{C}$ (3.1 kΩ),

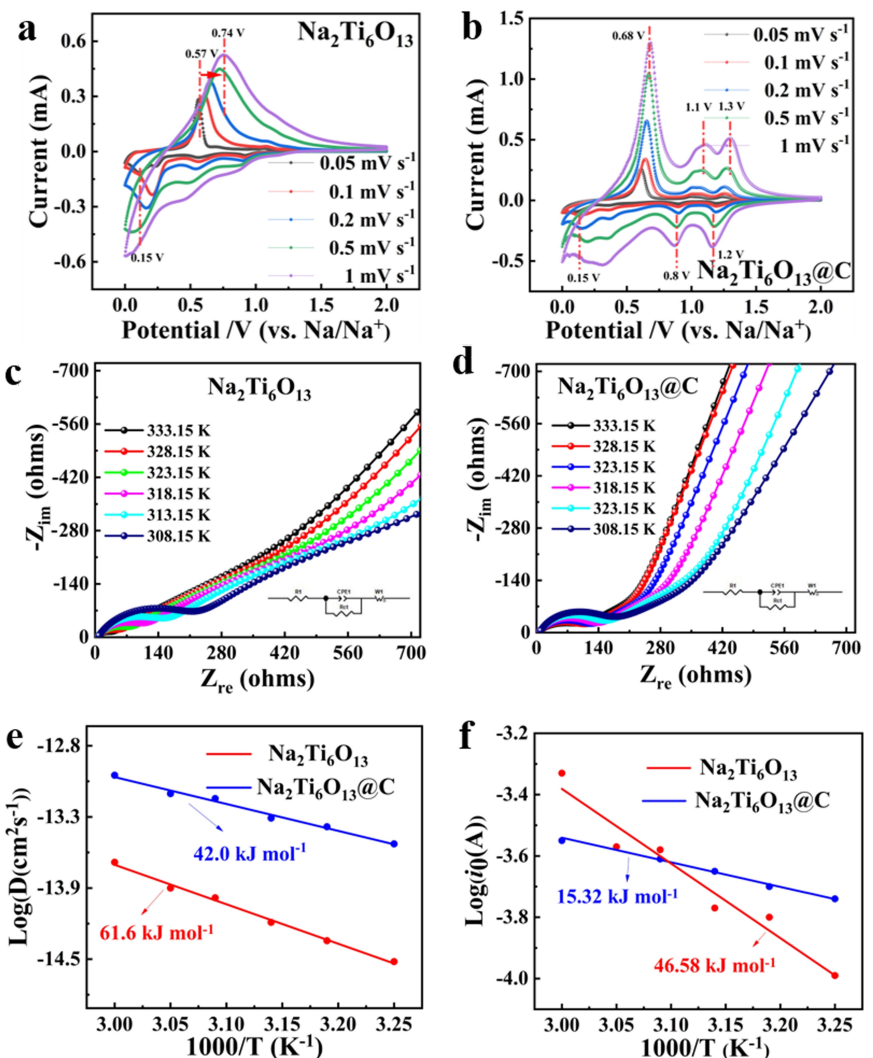


Figure 3. Cyclic voltammograms of a) $\text{Na}_2\text{Ti}_6\text{O}_{13}$ and b) $\text{Na}_2\text{Ti}_6\text{O}_{13}@C$ at different scan rates from 0.05 to 1 mV s^{-1} at 20°C . Nyquist plots of c) $\text{Na}_2\text{Ti}_6\text{O}_{13}$ and d) $\text{Na}_2\text{Ti}_6\text{O}_{13}@C$ electrode at $20, 30, 40, 50, 60^\circ\text{C}$. e) Arrhenius plots of $\log D_{\text{Na}^+}$ versus T^{-1} for the $\text{Na}_2\text{Ti}_6\text{O}_{13}$ and $\text{Na}_2\text{Ti}_6\text{O}_{13}@C$ electrodes; f) $\log i_0$ versus T^{-1} for the $\text{Na}_2\text{Ti}_6\text{O}_{13}$ and $\text{Na}_2\text{Ti}_6\text{O}_{13}@C$ electrodes during Na insertion.

indicating the interface of between $\text{Na}_2\text{Ti}_6\text{O}_{13}@C$ and electrolyte can effectively weaken the reaction energy barrier and improves the ion diffusion kinetics.^[40]

In order to characterize the full-cell electrochemical performance,^[41] it is necessary to assemble the sodium ion full-cell system coupling with sodium vanadium phosphate (NVP) as cathode and the obtained $\text{Na}_2\text{Ti}_6\text{O}_{13}@C$ as anode ($\text{Na}_2\text{Ti}_6\text{O}_{13}@C || \text{NVP}$). Figure 5(a) presents the charge/discharge profiles of the $\text{Na}_2\text{Ti}_6\text{O}_{13}@C || \text{NVP}$ at 0.1 C , an initial specific capacity of 141.7 mAh g^{-1} with a working voltage of 3.06 V is obtained. The CV curves are depicted in Figure 5(b). The redox peaks of full cell located at $2.75/3.25 \text{ V}$ at the scanning rate of 0.05 mVs^{-1} has no obvious peak shift during cycles, indicating a reversible redox activity and a small polarization. The reversible charge capacity achieves 75 mAh g^{-1} , 47 mAh g^{-1} , 36 mAh g^{-1} at 20°C , 0°C and -20°C , respectively (Figure 5c), remaining nearly 60% capacity at lower -20°C comparing to that at 20°C . As shown in Figure 5(d), the $\text{Na}_2\text{Ti}_6\text{O}_{13}@C || \text{NVP}$ exhibits an acceptable rate capability in the wide-temperature

range of from 20°C to -40°C without the special low-temperature electrolyte. As exhibited the cycle diagram of Figure 5(e), the capacity retention can still reach 65% after 175 cycles at 0°C . In general, the obtained $\text{Na}_2\text{Ti}_6\text{O}_{13}@C$ nanowires can realize an acceptable ion storage and diffusion behaviors at a low-temperature to -40°C , which can be considered as one of the most promising alternatives to hard carbon anode.

Conclusion

The tunnel-type $\text{Na}_2\text{Ti}_6\text{O}_{13}@C$ nanowires were synthesized and proposed to the low-temperature SIBs in this work. Beneficial to the inherent tunnel-type structure and ions diffusion pathway optimization, it can effectively attenuate apparent activation energy and intensified Na^+ diffusion coefficient. The kinetic analysis distinctly demonstrated that the diffusion apparent activation energy is 42.0 kJ mol^{-1} and the activation energy is $15.32 \text{ kJ mol}^{-1}$. The sodium ion diffusion coefficients

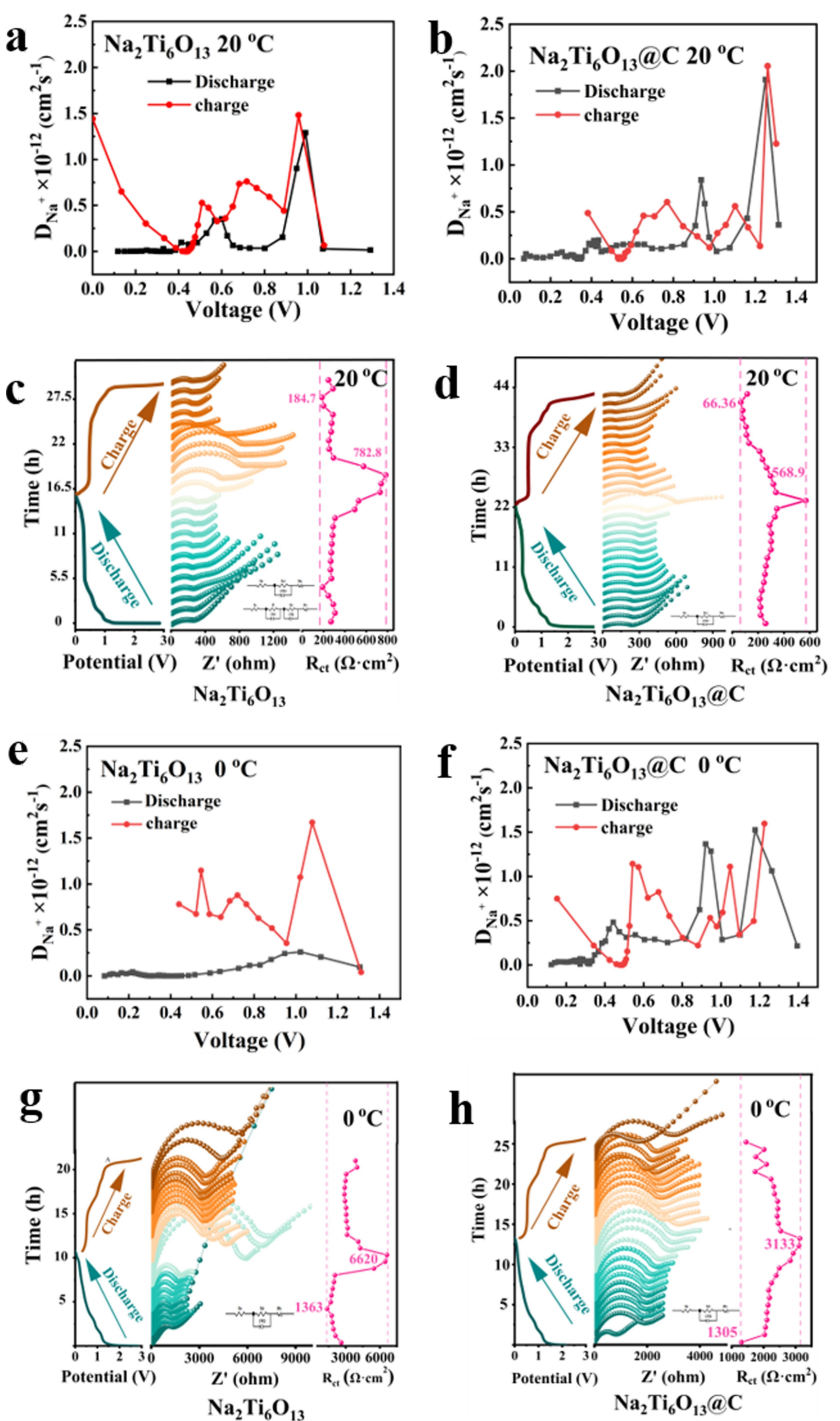


Figure 4. a and b) Na ion diffusivity versus state of charge-discharge calculated by GITT for $\text{Na}_2\text{Ti}_6\text{O}_{13}$ and $\text{Na}_2\text{Ti}_6\text{O}_{13}@\text{C}$ at 20°C. c and d) In situ electrochemical impedance spectroscopy (EIS) was employed to elucidate the transport kinetics during $\text{Na}_2\text{Ti}_6\text{O}_{13}$ and $\text{Na}_2\text{Ti}_6\text{O}_{13}@\text{C}$ electrode charge and discharge process in half cell at 20°C, the insets show the equivalent circuit. g and h) The GITT, and e and f) in-situ EIS at 0°C.

are calculated to be about $10^{-12} \text{ cm}^2 \text{s}^{-1}$ at 20°C and 0°C. The $\text{Na}_2\text{Ti}_6\text{O}_{13}@\text{C}$ performed a distinguished rate capability and a cycle stability at low working temperatures, with a favorable capacity retention closing to 100% after 200 cycles at 0.5 C under 0°C. Besides, the fabricated full cells ($\text{Na}_2\text{Ti}_6\text{O}_{13}@\text{C} \parallel \text{NVP}$) exhibited relatively superior performances at 0°C with a high-capacity retention nearly 65% after 175 cycles. For this work,

the explored tunnel-type $\text{Na}_2\text{Ti}_6\text{O}_{13}@\text{C}$ nanowires could provide a new approach to alternate hard carbon anode for the practical application of low-temperature SIBs.

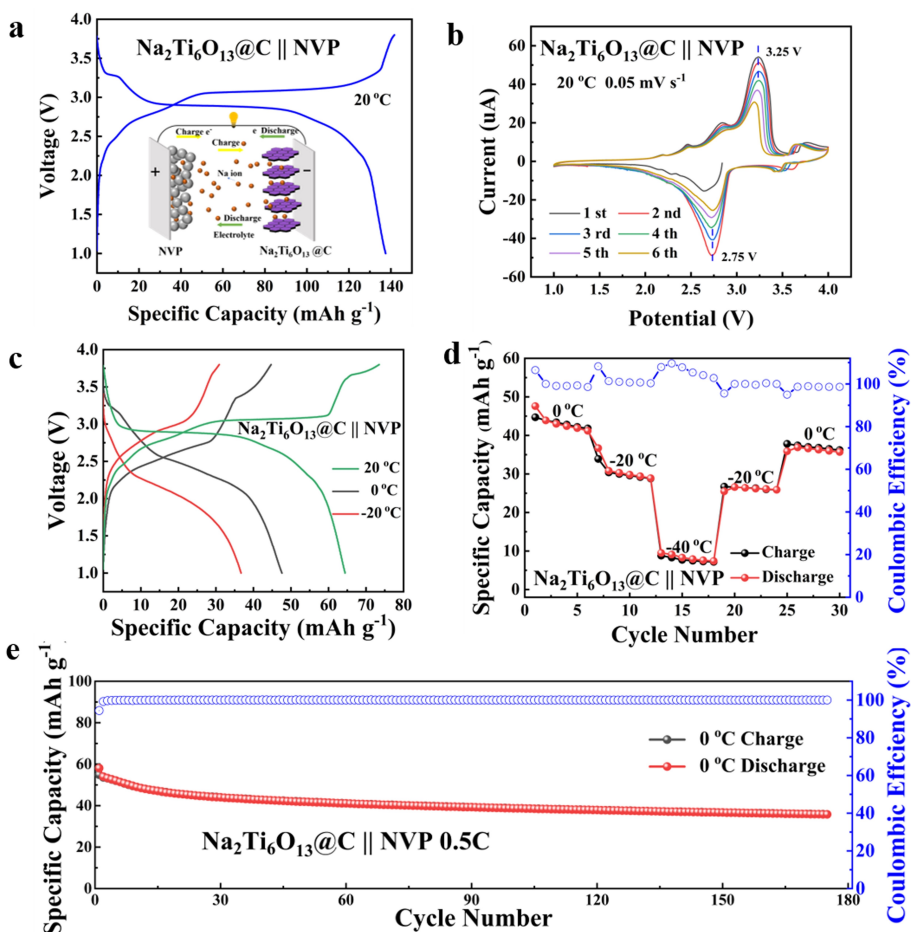


Figure 5. Electrochemical performance of full-cell coupling with $\text{Na}_2\text{Ti}_6\text{O}_{13}@\text{C}$ as anode and NVP as cathode. a) Typical galvanostatic charge-discharge (GCD) curves at 0.1 C rate in the voltage range of 1.0–3.8 V. The inset is the schematic diagram of NVP || $\text{Na}_2\text{Ti}_6\text{O}_{13}@\text{C}$ full-cell. (b) Cyclic voltammograms at 0.05 mV s⁻¹ of NVP || $\text{Na}_2\text{Ti}_6\text{O}_{13}@\text{C}$; c) GCD curves of different temperatures at 0.5 C. d) Cycle performance of different low temperature at 0.5 C. e) Long-term cycle performance at 0.5 C with 0 °C of the sodium-ion full cell.

Experimental Section

Preparation of the $\text{Na}_2\text{Ti}_6\text{O}_{13}$: The precursor of $\text{Na}_2\text{Ti}_6\text{O}_{13}$ was prepared via hydrothermal method. Firstly, titanium dioxide powder (99.8% metal basis) was dispersed in 7 mol L⁻¹ NaOH (AR, 95%) aqueous solution with 30 min sonication treatment. The suspension solution was then placed in a 100 mL stainless steel autoclave and heated at 200 °C in oven for 48 h. The white hydrate sodium titanate precursor was obtained after washing several times and dried in oven overnight. $\text{Na}_2\text{Ti}_6\text{O}_{13}$ was synthesized by annealing precursor powder at 600 °C with the rate of 5 °C min⁻¹ for 3 h.

Preparation of the $\text{Na}_2\text{Ti}_6\text{O}_{13}@\text{C}$: The $\text{Na}_2\text{Ti}_6\text{O}_{13}@\text{C}$ was synthesized through the chemical vapor deposition (CVD) method. Firstly, as-synthesized $\text{Na}_2\text{Ti}_6\text{O}_{13}$ powders were placed in the tube furnace, then heated to 600 °C at the rate of 5 °C min⁻¹ under Ar and C_2H_2 mixture (the weight ratio of C_2H_2 and Ar is 2:8). The vapor deposition process lasted 0.5 h to obtain $\text{Na}_2\text{Ti}_6\text{O}_{13}@\text{C}$ sample.

Preparation of sodium vanadium phosphate (NVP): Sodium vanadium phosphate (NVP) was prepared by the typical sol-gel method.^[42,43] First, 0.72 g vanadium pentoxide and 1.52 g oxalic acid were stirred in deionized water (40 mL, H_2O) at 70 °C for 1 hour. Then, 1.84 g sodium phosphate monobasic and 0.4 g glucose were added and dissolved in the solution with stirring for 10 min. The 100 mL n-propanol solution was added under

continuously stirring for 0.5 h. After dried in an oven for overnight, the product was preheated at 350 °C for 4 h and annealed at 800 °C for 6 hours in H₂/Ar atmosphere.

Material characterizations: The crystalline phase of the synthesized sample is confirmed by the Rigaku-T III X-ray diffractometer (XRD, equipped with Cu K_α radiation = 1.5406 Å, Shimadzu X-ray 6000). Scanning electron microscope (SEM; Hitachi S-4800; accelerating voltage of 5.0 kV) is used to perform the morphology of samples. Transmission electron microscopy (TEM; JEM-2100; accelerating voltage of 200 kV) is used to characterize the crystal structure of $\text{Na}_2\text{Ti}_6\text{O}_{13}@\text{C}$ nanorods. Elemental distributions were measured by the energy dispersive spectrometer (EDS) mapping analysis. The valence state of element of samples are characterized by a Large Area XL X-ray photoelectron spectroscopy (XPS, equipped with 150 W Al K Alpha radiation).

Electrochemical tests: The electrochemical performances of $\text{Na}_2\text{Ti}_6\text{O}_{13}@\text{C}$ and $\text{Na}_2\text{Ti}_6\text{O}_{13}$ as anode electrodes were evaluated by fabricating the CR2032 coin-type cells. The working electrodes was prepared by coating the slurry on Al foil, which contains active material, acetylene carbon black and sodium carboxymethyl cellulose (CMC) (8:1:1 in weight). The average weight of the obtained active material on each piece was about 2.0 mg. The NVP electrode was prepared by coating the slurry on Al foil, which contains active material, super P, and polyvinylidene fluoride

binder (PVDF) (7:2:1 in weight). The assembled process of the coin cells was carried out in a dry Ar-filled glove box. Sodium served as the counter electrode, and the glass fiber membrane was used as the separator. The commercialized electrolyte of 1 M NaClO₄ in EC/DEC solvent (1:1 v/v) with 5 wt.% fluoroethylene carbonate (FEC) was employed. The capacity mass ratio of anode and cathode was from 1 to 1.5. The full cell of active material was calculated based on NVP. Before the cycle ratio test at low temperature, three activation cycles were carried out at room temperature. Sodium vanadium phosphate and A were loaded into half batteries respectively for 5 activation cycles, and then the whole battery test was carried out at low temperature. The galvanostatic charge-discharge test were presented by LAND-CT2001 A battery testing system under different current densities from 0.1 C to 5 C (all nominal capacity used in tests is 100 mAh g⁻¹) between 0.01 and 3 V vs. Na⁺/Na from 20°C to -40°C. The EIS tests (Princeton Applied Research PARSTAT 2273) were carried with an AC amplitude of 10 mV in the frequency domain 100 kHz to 10 mHz. The EIS test is performed under six different temperatures (35, 40, 45, 50, 55 and 60°C) to evaluate the impedance and apparent activation energy of the battery. Cyclic voltammeter (CV) and Galvanostatic intermittent titration technique (GITT) were presented by electrochemical Workstation (Princeton Applied Research PARSTAT 2273).

The impedance curve shows a semicircle in intermediate frequency area, which represents the reaction resistance. The oblique straight line in the low frequency area, which represents the Warburg impedance.^[44] The experimental result was calculated using the equivalent circuit. To quantify the dynamics of electrode materials, the exchange current (i_0) and the apparent activation energy (E_a) were calculated from Equations (1) and (2) (Arrhenius equation),^[31,32]

$$i_0 = RT/nFRct \quad (1)$$

$$i_0 = A\exp(-E_a/RT) \quad (2)$$

in which, A is the area where the electrode is in contact with the electrolyte, R is the constant, T is temperature, n is the number of diffusion electrons, and F is the Faraday constant.

The Na⁺ diffusion coefficient can be fitted by Equation (3)^[2]

$$D = R^2 T^2 / 2A^2 n^4 F^4 C^2 \sigma^2 \quad (3)$$

where C is the concentration of Na⁺ in the solid, which can be calculated by Equation (4), D is the Na⁺ diffusion coefficient, and σ is the Warburg factor, which can be calculated by Equation (5) in the slope of the lines in Figure S3.

$$C = \rho/M \quad (4)$$

$$Z_{re} = R_s + R_f + R_{ct} + \sigma\omega^{-1/2} \quad (5)$$

Figure 3(e) demonstrates the diagram of log D as a function of T^{-1} , according to Z_{re} versus $\omega^{1/2}$ at different temperatures. The diffusion apparent activation energy (E_{aD}) can be gained for 42.0 and 61.6 kJ mol⁻¹ of the Na₂Ti₆O₁₃@C and Na₂Ti₆O₁₃ by Equation (6):

$$E_{aD} = -RK\ln 10 \quad (6)$$

in Equation (6), K is the slope of the fitting line in Figure 3(e).

The activation energies (E_a) can be calculated by Equation (7):

$$E_a = -RK\ln 10 \quad (7)$$

in Equation (7), K is the slope of the fitting line in Figure 3(f).

the Na ion diffusion coefficients D_{Na^+} were calculated by Equation (8):

$$D_{Na^+} = \frac{4}{\pi} \left(\frac{m_B V_M}{M_B A} \right) \left(\frac{\Delta E}{dE_\tau/d\sqrt{\tau}} \right)^2 \left(\tau \ll \frac{L^2}{D_{Na^+}} \right) \quad (8)$$

in Equation (8), V_M is the molar volume of materials, M_B is the relative molecular mass of material, m_B is the quality of material, A is the electrode area, L is the thickness of material, τ is relaxation time, and ΔE is open circuit voltage, $dE_\tau/d\sqrt{\tau}$ can be gained from a plot of Figure S4(a-d). In the test process, if the voltage and time are linear ordered relation, Equation (8) can be simplified to Equation (9).

$$D_{Na^+} = \frac{4}{\pi} \left(\frac{m_B V_M}{M_B A} \right) \left(\frac{\Delta E}{\Delta E_\tau} \right)^2 \quad (9)$$

where ΔE_τ is Battery voltage difference at the beginning and end of the current pulse.

Supporting Information

XRD, SEM, and more electrochemical data, including EIS, CV, and charge/discharge curves are provided in the Supporting Information. Supporting Information is available from the Wiley Online Library or from the author.

Acknowledgements

This work was supported by the National Natural Science Foundation of China (Grant No. 52272194, 52204308), LiaoNing Revitalization Talents Program (No. XLYC2007155), the Fundamental Research Funds for the Central Universities (N2025018, N2025009). China Postdoctoral Science Foundation (2022 M710639).

Conflict of Interest

The authors declare no conflict of interest.

Data Availability Statement

The data that support the findings of this study are available on request from the corresponding author. The data are not publicly available due to privacy or ethical restrictions.

Keywords: anode · low-temperature · Na₂Ti₆O₁₃@C nanowires · sodium-ion batteries · tunnel-type structure

- [1] H. Pan, X. Lu, X. Yu, Y.-S. Hu, H. Li, X.-Q. Yang, L. Chen, *Adv. Energy Mater.* **2013**, *3*, 1186–1194.
- [2] H. Pan, Y.-S. Hu, L. Chen, *Energy Environ. Sci.* **2013**, *6*, 2338–2360.
- [3] Y. Wen, K. He, Y. Zhu, F. Han, Y. Xu, I. Matsuda, Y. Ishii, J. Cumings, C. Wang, *Nat. Commun.* **2014**, *5*, 4033.
- [4] D. Zhao, S. Jiang, S. Yu, J. Ren, Z. Zhang, S. Liu, X. Liu, Z. Wang, Y. Wu, Y. Zhang, *Carbon* **2023**, *201*, 864–870.
- [5] D. Zhao, S. Ge-Zhang, Z. Zhang, H. Tang, Y. Xu, F. Gao, X. Xu, S. Liu, J. Zhou, Z. Wang, Y. Wu, X. Liu, Y. Zhang, *ACS Appl. Mater. Interfaces* **2022**, *14* (49), 54662–54669.
- [6] W. Lv, C. Zhu, J. Chen, C. Ou, Q. Zhang, S. Zhong, *Chem. Eng. J.* **2021**, *418*, 129400.
- [7] S. Tan, U. N. D. Rodrigo, Z. Shadike, B. Lucht, K. Xu, C. Wang, X. Q. Yang, E. Hu, *ACS Appl. Mater. Interfaces* **2021**, *13*, 24995–25001.
- [8] K. Zhu, Z. Sun, T. Jin, X. Chen, Y. Si, H. Li, L. Jiao, *Batteries & Supercaps* **2022**, *5*, e202200308.
- [9] K. Richter, T. Waldmann, N. Paul, N. Jobst, R.-G. Scurtu, M. Hofmann, R. Gilles, M. Wohlfahrt-Mehrens, *ChemSusChem* **2020**, *13*, 529–538.
- [10] D. Zhao, Z. Zhang, J. Ren, Y. Xu, X. Xu, J. Zhou, F. Gao, H. Tang, S. Liu, Z. Wang, D. Wang, Y. Wu, X. Liu, Y. Zhang, *Chem. Eng. J.* **2023**, *451*, 138882.
- [11] N. Zhang, T. Deng, S. Zhang, C. Wang, L. Chen, C. Wang, X. Fan, *Adv. Mater.* **2022**, *34*, e2107899.
- [12] W. Jia, Y. Liu, Z. Wang, F. Qing, J. Li, Y. Wang, R. Xiao, A. Zhou, G. Li, X. Yu, Y.-S. Hu, H. Li, Z. Wang, X. Huang, L. Chen, *Sci. Bull.* **2020**, *65*, 1907–1915.
- [13] J. Zhang, L. Lai, H. Wang, M. Chen, Z. X. Shen, *Mater. Today Energy* **2021**, *21*, 100747.
- [14] L. F. Zhou, X. W. Gao, T. Du, H. Gong, L. Y. Liu, W. B. Luo, *Chem. Eng. J.* **2022**, *435*, 134838.
- [15] Y. Sun, Y. Zhang, Z. Xu, W. Gou, X. Han, M. Liu, C. M. Li, *ChemSusChem* **2022**, *15*, e202201362.
- [16] S.-D. Lee, K.-N. Jung, H. Kim, H.-S. Shin, S.-W. Song, M.-S. Park, J.-W. Lee, *ChemSusChem* **2017**, *10*, 2175–2181.
- [17] S. Yuan, X. Duan, J. Liu, Y. Ye, F. Lv, T. Liu, Q. Wang, X. Zhang, *Energy Storage Mater.* **2021**, *42*, 317–369.
- [18] X. Ge, Y. Zhu, Z. Cao, J. Jia, Q. Zhao, S. Chang, S. Liu, X. Yang, K. Feng, *J. Alloys Compd.* **2022**, *903*, 163914.
- [19] B. Papandrea, X. Xu, Y. Xu, C.-Y. Chen, Z. Lin, G. Wang, Y. Luo, M. Liu, Y. Huang, L. Mai, X. Duan, *Nano Res.* **2016**, *9*, 240–248.
- [20] Y. Wang, N. Xiao, Z. Wang, H. Li, M. Yu, Y. Tang, M. Hao, C. Liu, Y. Zhou, J. Qiu, *Chem. Eng. J.* **2018**, *342*, 52–60.
- [21] X. Cheng, D. Li, Y. Wu, R. Xu, Y. Yu, J. Mater. Chem. A **2019**, *7*, 4913–4921.
- [22] A. Rudola, K. Saravanan, C. W. Masona, P. Balaya, *J. Mater. Chem. A* **2013**, *1*, 2653–2662.
- [23] J. Ni, S. Fu, C. Wu, Y. Zhao, J. Maier, Y. Yu, L. Li, *Adv. Energy Mater.* **2016**, *6*, 1502568.
- [24] B. Deng, N. Yue, H. Dong, Q. Gui, L. Xiao, J. Liu, *Chin. Chem. Lett.* **2021**, *32*, 826–829.
- [25] X. Feng, H.-H. Wu, B. Gao, M. Świętosławski, X. He, Q. Zhang, *Nano Res.* **2021**, *15*, 352–360.
- [26] M. Cai, H. Zhang, Y. Zhang, B. Xiao, L. Wang, M. Li, Y. Wu, B. Sa, H. Liao, L. Zhang, S. Chen, D.-L. Peng, M.-S. Wang, Q. Zhang, *Sci. Bull.* **2022**, *67*, 933–945.
- [27] Y. Xia, L.-F. Que, F.-D. Yu, L. Deng, C. Liu, X.-L. Sui, L. Zhao, Z.-B. Wang, *Chem. Eng. J.* **2021**, *404*, 127116.
- [28] Q. Meng, Y. Lu, F. Ding, Q. Zhang, L. Chen, Y.-S. Hu, *ACS Energy Lett.* **2019**, *4*, 2608–2612.
- [29] H. Huang, R. Xu, Y. Feng, S. Zeng, Y. Jiang, H. Wang, W. Luo, Y. Yu, *Adv. Mater.* **2020**, *32*, e1904320.
- [30] M. Mandl, J. Becherer, D. Kramer, R. Mönig, T. Diermant, R. J. Behm, M. Hahn, O. Böse, M. A. Danzer, *Electrochim. Acta* **2020**, *354*, 136698.
- [31] S.-L. Chou, J.-Z. Wang, H.-K. Liu, S.-X. Dou, *J. Phys. Chem. C* **2011**, *115*, 16220–16227.
- [32] W.-B. Luo, S.-L. Chou, Y.-C. Zhai, L. H.-K. Liu, *J. Mater. Chem. A* **2014**, *2*, 4927–4931.
- [33] W. Ren, L. Xiong, X. Yuan, Z. Yu, H. Zhang, X. Duan, S. Wang, *Environ. Sci. Technol.* **2019**, *53*, 14595–14603.
- [34] F. Gao, B. Mei, X. Xu, J. Ren, D. Zhao, Z. Zhang, Z. Wang, Y. Wu, X. Liu, Y. Zhang, *Chem. Eng. J.* **2022**, *448*, 137742.
- [35] X. Shen, Q. Zhou, M. Han, X. Qi, B. Li, Q. Zhang, J. Zhao, C. Yang, H. Liu, Y. S. Hu, *Nat. Commun.* **2021**, *12*, 2848.
- [36] J. Deng, W.-B. Luo, X. Lu, Q. Yao, Z. Wang, H.-K. Liu, H. Zhou, S.-X. Dou, *Adv. Energy Mater.* **2018**, *8*, 1701610.
- [37] M. Li, Z. Zuo, J. Deng, Z. Wang, S.-X. Dou, *J. Mater. Chem. A* **2018**, *6*, 9962–9970.
- [38] M. Li, Z.-I. Zuo, J.-Q. Deng, Q.-R. Yao, Z.-M. Wang, H.-Y. Zhou, W.-B. Luo, H.-K. Liu, S.-X. Dou, *J. Mater. Chem. A* **2018**, *6*, 9962–9970.
- [39] W. Shen, H. Li, Z.-Y. Guo, C. Wang, Z.-H. Li, Q.-J. Xu, H.-m. Liu, Y.-g. Wang, Y.-y. Xia, *ACS Appl. Mater. Interfaces* **2016**, *8*, 15341–15351.
- [40] C. Ke, R. Shao, Y. Zhang, Z. Sun, S. Qi, H. Zhang, M. Li, Z. Chen, Y. Wang, B. Sa, H. Lin, H. Liu, M. S. Wang, S. Chen, Q. Zhang, *Adv. Funct. Mater.* **2022**, *32*, 2205635.
- [41] L. Zhao, H. Yang, F. He, Y. Yao, R. Xu, L. Wang, L. He, H. Zhang, S. Li, F. Huang, *Electrochim. Acta* **2021**, *388*, 138565.
- [42] Y. Jiang, X. Zhou, D. Li, X. Cheng, F. Liu, Y. Yu, *Adv. Energy Mater.* **2018**, *8*, 1800068.
- [43] Z. Liu, J. Wang, B. Lu, *Sci. Bull.* **2020**, *65*, 1242–1251.
- [44] M. Messing, T. Shoa, S. Habibi, *J. Energy Storage* **2021**, *43*, 103210.

Manuscript received: December 16, 2022

Revised manuscript received: January 13, 2023

Version of record online: March 1, 2023